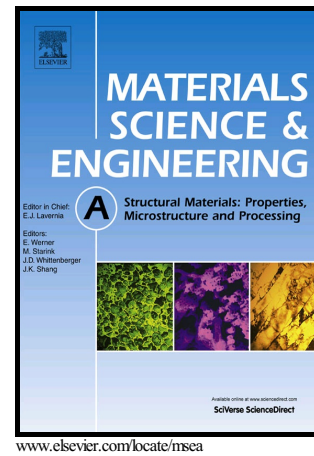# Author's Accepted Manuscript

Stability of retained austenite in martensitic high carbon steels. Part I: Thermal stability

Wen Cui, David San-Martín, Pedro E.J. Rivera-Díaz-del-Castillo

Cite this article as: Wen Cui, David San-Martín and Pedro E.J. Rivera-Díaz-del-Castillo, Stability of retained austenite in martensitic high carbon steels. Part I: Thermal stability, *Materials Science & Engineering A,* https://doi.org/10.1016/j.msea.2017.10.102

Stability of retained austenite in martensitic high carbon steels. Part I: Thermal stability

Wen Cui[a], David San-Martín[b], Pedro E.J. Rivera-Díaz-del-Castillo[c,*]

[a]*SKF University Technology Centre, Department of Materials Science and Metallurgy, University of Cambridge, 27 Charles Babbage Road, Cambridge, CB3 0FS, UK*
[b]*MATERALIA Research Group, Department of Physical Metallurgy, Centro Nacional de Investigaciones Metalurgicas (CENIM-CSIC), Av. Gregorio del Amo 8, 28040 Madrid, Spain*
[c]*Department of Engineering, Lancaster University, Lancaster, LA1 4YW, UK*

Abstract

Thermal stability of retained austenite in 1C-1.5Cr steels with two Si and Mn contents is studied. Time-resolved high resolution synchrotron X-ray radiation and dilatometry are employed. The threshold transformation temperatures, decomposition kinetics, associated transformation strain, as well as the influence of Si and Mn were investigated. The coefficients of linear thermal expansion for both the bulk materials and individual phases are also obtained. The results indicate that an increase in the Mn and Si contents show little influence on the onset of retained austenite decomposition, but result in more thermally stable austenite. The decomposition is accompanied by a simultaneous increase in ferrite content which causes an expansive strain in the order of 10^{-4}, and subsequent cementite development from 300–350 °C which causes a contraction that helps to neutralise the expansive strain. During decomposition, a continuous increase in the carbon content of austenite, and a reduction in that of the tempered-martensite/ferrite phase was observed. This process continued at elevated temperatures until full decomposition was reached, which could take less than an hour at a heating rate of 0.05 °C/s. Additionally, the observation of austenite peak splitting on samples with high Mn and Si contents suggests the existence of austenite of different stabilities in such matrix.

Keywords: Austenite, Phase stability, Synchrotron radiation, Dilatometry, Martensitic

*Corresponding author
Email address: `p.rivera1@lancaster.ac.uk` (Pedro E.J. Rivera-Díaz-del-Castillo)

bearing steels

1. Introduction

Precise control of steel properties relies on its microstructural stability. The presence of austenite, however, causes uncertainty. Being thermodynamically metastable, austenite retained at room temperature could decompose via either thermally- or mechanically-induced phase transformations. Such metastability has played a key role in controlling the strength and toughness in hypoeutectoid steels with carbon content less than 0.6 wt.%, for instance ausformed steels [1, 2, 3, 4] and TRIP-assisted steels [4, 5, 6], whilst less has been explored on hypereutectoid steels.

Hypereutectoid steels are extensively used for applications which require very high strength. Those with a base composition of 1C-1.5Cr (wt.%) are the prevalent material for bearing applications in a variety of rotating machinery such as gearboxes and aircraft engines. These materials are subjected to multi-step heat treatments, typically consisting of austenitisation, quenching and tempering, to obtain a martensite structure for desired hardness. Due to the high carbon content which depresses the martensite start temperature, alloys of this kind contain typically 5–10 wt.% retained austenite after heat treatment. Much attention has been devoted to retained austenite stability, as its decomposition may on the one hand be detrimental to bearing dimensional stability [7, 8, 9, 10], but on the other hand enhance bearing rolling contact fatigue life under various test conditions, e.g. contact pressures up to 3 GPa, stress cycles reaching 10^7 and in debris contaminated lubricant [11, 12, 13]. In addition, stable retained austenite has shown a beneficial effect on bearing performance under contaminated lubrication operation [14].

During rolling contact, the cyclic rolling of elements unavoidably causes an accumulation of contact stresses, such stress is a combination of compression and shear [15, 16] and can typically reach 3 GPa [17]. In addition to stress accumulation, there may be temperature increase and gradients across the stressed area, especially under non-ideal lubrication condi-

tions. Kannel and Barber [18] have predicted temperature may rise from 56 °C up to 500 °C after 1200 s rolling contact, caused by slippage between roller and race during rolling contact. As a result, retained austenite decomposition will likely occur progressively due to localised accumulation of temperature and/or stress, understanding of which requires knowledge on both the thermal and mechanical stability of retained austenite. Whilst considerable amount of evidence on retained austenite decomposition has been reported [11, 12, 13, 19, 20, 21, 22], early studies are limited to conventional X-ray diffraction and microscopy techniques which show only snapshots of the retained austenite transforamtion. A recent study [23] has revealed the carbon redistribution path associated with the decomposition of retained austenite using time-resolved synchrotron X-ray radiation, the study, however, focuses on retained austenite decomposition at temperatures up to ~200 °C, and under the application of a constant tensile stress. The threshold temperatures for retained austenite decomposition, transformation-induced strain and influence of substitutional alloying elements on retained austenite stability are not fully understood. Also, retained austenite stability under cyclic compression and material response are rarely reported.

The present work aims at investigating the stability of retained austenite upon increasing temperatures and number of compressive stress cycles in two popular martensitic bearing steel grades 100Cr6 and 100CrMnSi6-4, their chemical compositions are given in Table 1. Whilst 100Cr6 is commonly employed for small to medium bearing applications, 100CrMnSi6-4 allows greater hardenability due to its relatively high Mn and Si contents and can be utilised for medium to large components [24]. In the first part of the work, the *in situ* thermal stability of retained austenite whilst gradually increasing temperature is studied, as well as its decomposition mechanisms and the associated transformation-induced strain,

Table 1: Initial chemical composition of steels (wt.%) as reported by the supplier.

Grade	C	Cr	Mn	Si	Cu	Ni	Mo	Al	Fe
100Cr6	0.99	1.48	0.35	0.25	0.15	0.13	0.05	0.03	Bal.
100CrMnSi6-4	0.99	1.53	1.10	0.6	0.15	0.13	0.05	0.03	Bal.

employing dilatometry and time-resolved high-resolution synchrotron X-ray radiation. The study also highlights the influence of Mn and Si alloying elements on retained austenite thermal stability. In the accompanying paper, cyclic compression is adopted to study its mechanical stability and *in situ* material stress-strain response combining X-ray diffraction and repetitive push testing, and interpreted in light of finite element method calculations.

2. Experimental

2.1. Heat treatments and microstructural investigation

Heat treatment consisting of austenitisation, two-step-quenching and tempering was performed in an Adamel-Lhomargy DT1000 high-resolution dilatometer, with temperatures monitored by a thermocouple attached to each specimen. Austenitisation was carried out by heating to a selected temperature (T_{aus}) at a rate of 1 °C/s and subsequent holding at that temperature for 30 min. Quenching to 70 °C and subsequently to 10 °C took place at rates of -50 °C/s and -5 °C/s, respectively, with the specimens being held 5–10 min at such temperatures. Tempering was then performed at 160 °C for 2 h with a heating rate of 1 °C/s to reach such temperature followed by cooling at -5 °C/s to room temperature. 100Cr6 specimens were austenitised at 820, 860 and 900 °C, whilst 100CrMnSi6-4 were austenitised at 800, 840 and 880 °C. This aims at obtaining retained austenite of identical chemical driving force and the same phase quantity upon quenching in the two grades [25].

Metallographic characterisation was carried out using a Leica DM 2500M optical microscope. All samples were mechanically ground using grit SiC papers progressively down to 2500, followed by fine polishing on a napped cloth using 6 m and 1 m diamond paste, prior to etching in 2% nital.

2.2. Dilatometry

Dilatometric experiments to examine retained austenite stability were performed in an Adamel-Lhomargy DT1000 dilatometer. One sample was prepared for each test. Specimens were rods of 2 mm diameter and 12 mm length. The martensitic specimens described in the

4

previous section were subsequently heated to 350 °C at 0.05 °C/s and held for 20 min before being cooled to room temperature at −0.05 °C/s.

2.3. Synchrotron

2.3.1. Experimental configuration

Synchrotron experiments to examine retained austenite stability were performed on the high-resolution powder diffraction I11 beamline [26] at Diamond Light Source (Didcot, UK). The experiment was operated at the optimised energy of the beamline 15 keV, resulting in a penetration depth of ∼22.8 μm into the bulk material, in contrast to 4.25 μm for a conventional laboratory X-ray facility employing 8 keV Cu Kα radiation. The calculation of the depths is given in the supplementary material. Prior to the experiment, the wavelength and zero point (error in 2θ) was calibrated to be 0.826225 Å and -0.040379(1)°, respectively, using a standard Si sample. The default beam size of 0.5 mm vertical and 2.5 mm horizontal was used. Data were collected by a position sensitive detector (PSD), which uses Mython-2 Si strip modules with a slit width of 0.05 mm and allows time-resolved analysis.

Capillary samples of 0.5 mm diameter and 7 mm length were prepared for *in situ* synchrotron studies. For obtaining such specimen, spheroidised bars were initially machined and ground into a designed form shown in Figure 1a. This was done before heat treatment for the ease of machining. The thick end with a diameter of 2.5 mm is required by the dilatometer for conducting the heat treatments. The middle part with a diameter of 1.5 mm is designed to prevent the sample from breaking during grinding or heat treatment. The needle section was cut off as a capillary sample after heat treatment.

Each specimen was located at the tip of a quartz capillary tube with an internal diameter 0.5–0.7 mm, Figure 1b. The tube was then filled with glass powder to avoid sample wobbling, sealed with superglue and mounted on a brass holder, which was then horizontally and magnetically attached onto a spinner equipped on the machine, allowing the sample to be positioned in the illumination area, Figure 1c. This way, the sample is well isolated from the brass holder which could either potentially generate impurity peaks in the diffraction spec-

trum, or cause heat losses due to the high thermal conductivity if directly being attached to the sample. The alignment of the sample to the beam position was adjusted under spinning, using two cameras with built-in cross hairs, to ensure full time illumination during experiment. Reference samples for each capillary sample were prepared for benchmark purposes, and one sample with only glass powder in the tube was prepared to get a spectrum for the sample holder.

Room temperature spectra were first collected for all samples. Each sample was then studied *in situ* under continuous heating using a Cyberstar hot-air blower. As shown in Figure 1d, samples were initially held at 130 °C for 10 min to ensure temperature homogeneity, then heated up to 500 °C at 0.05–0.09 °C/s. Within such temperature range, the samples were held at selected temperatures for 3 min to reach a steady state. They were then held at 500°C for 5 min and cooled at the maximum achievable rate of 0.16 °C/s. Diffraction patterns were collected at an exposure time of 30 s at selected points, marked as black diamonds in Figure 1d.
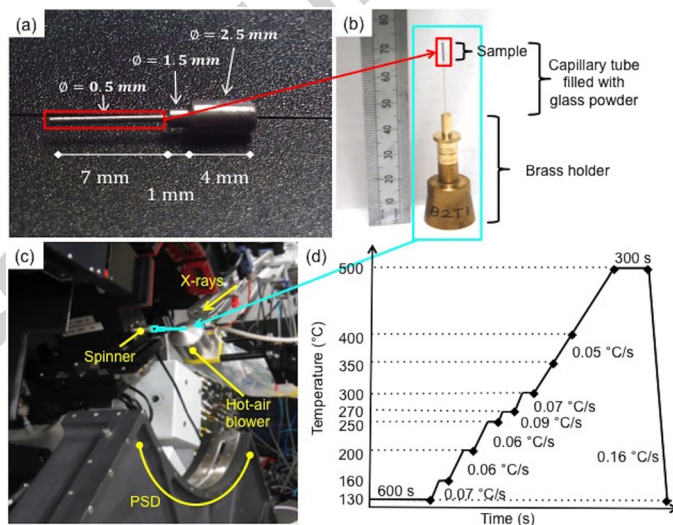

Figure 1: Illustration of (a) preliminary sample preparation for obtaining capillary specimen, (b) capillary sample assembling, (c) experimental setup at the I11 beamline, Diamond Light Source and (d) schematic of the *in situ* synchrotron experimental procedure.

6

2.3.2. Data analysis

Diffraction spectra were recorded directly as one-dimension (1-D) intensity *versus* diffracted angle 2θ data. The room temperature spectra cover a 2θ range of 15–105°, whilst others were collected up to 70° as the hot air blower blocks part of the detector. Nevertheless, as least five peaks were detectable under 70° for each present phase. Spectra were qualitatively and quantitatively analysed employing Bruker TOPAS c.4.2 via Rietveld refinement [27]. Crystallographic information files for ferrite, austenite, and Fe_3C from Fruchart *et al.* [28] were used for phase identification. As-tempered martensite peaks were fitted with a body-centred cubic structure, they were referred to as ferrite (α) peaks in this study.

Lattice parameters of austenite and ferrite were obtained directly from Rietveld refinement, which considers the position of all peaks detected for each phase, and estimates the lattice parameter for austenite and ferrite using Bragg's Law:

$$2d_{hkl} \sin \theta_{hkl} = \lambda \tag{1}$$

and the planar equation:

$$\frac{1}{d_{hkl}^2} = \frac{h^2 + k^2 + l^2}{a^2} \tag{2}$$

where d_{hkl} is the inter-planar distance between the hkl planes of atoms in the lattice; θ is the Bragg angle at which there is a maximum in diffracted intensity; λ is the wavelength of the incident beam; a is the lattice parameter for a cubic structure, and hkl are the Miller indices.

Carbon concentrations were empirically determined from the lattice parameters, for ferrite, using Equation [23]:

$$a_\alpha(\text{nm}) = 0.28664 + 0.002C_C + 0.000055C_{Mn} \tag{3}$$

where 0.28664 nm is the room temperature lattice parameter for pure BCC-iron [29, 30]. C_i in wt.% is the chemical composition of the subscripted element; and for austenite via

Equation [23, 31]:

$$a_\gamma(\text{nm}) = 0.3556 + 0.00006C_{Cr} + 0.000095C_{Mn} + 0.00453C_C \qquad (4)$$

where 0.3556 nm is widely considered to be the lattice parameter for pure FCC-iron [4].

The values for C_{Cr} and C_{Mn} were taken from kinetic calculations performed using Mat-Calc v.5.52 [32] with thermodynamic database mc_fe and diffusion database mc_fe_v2.001, as summarised in Table 2. The detailed calculation method is reported in [25]. It was assumed that C_{Cr} and C_{Mn} remain constant in all phases during quenching and tempering, and were identical in the quenched and tempered martensite to its parent prior-austenite. The effect of Si is reported to be negligible on the austenite lattice [33, 34] and only causes a small contraction of $0.00003C_{Si}$ nm for ferrite [30]. It was therefore not considered for the calculation. The impact of the other elements on the lattice parameter were considered to be negligible due to their small contents.

Table 2: Concentrations (wt.%) of Cr and Mn in the austenite phase of heat-treated samples, calculated via the MatCalc software.

	100Cr6			100CrMnSi6-4		
	820 °C	860 °C	900 °C	800 °C	840 °C	880 °C
Cr	0.86	1.11	1.28	0.89	1.05	1.23
Mn	0.26	0.29	0.32	0.80	0.88	0.96

3. Results and discussion

3.1. Microstructure

Optical micrographs in Figure 2 show the microstructure of all samples after heat treatment. Martensite and retained austenite matrix are present as dark and grey regions in the micrographs, and cementite was identified as white particles. An increase in T_{aus} promotes the growth of prior-austenite grains and the dissolution and cementite, resulting in the observation of a coarser microstructure and less cementite than samples austenitised at low T_{aus}.
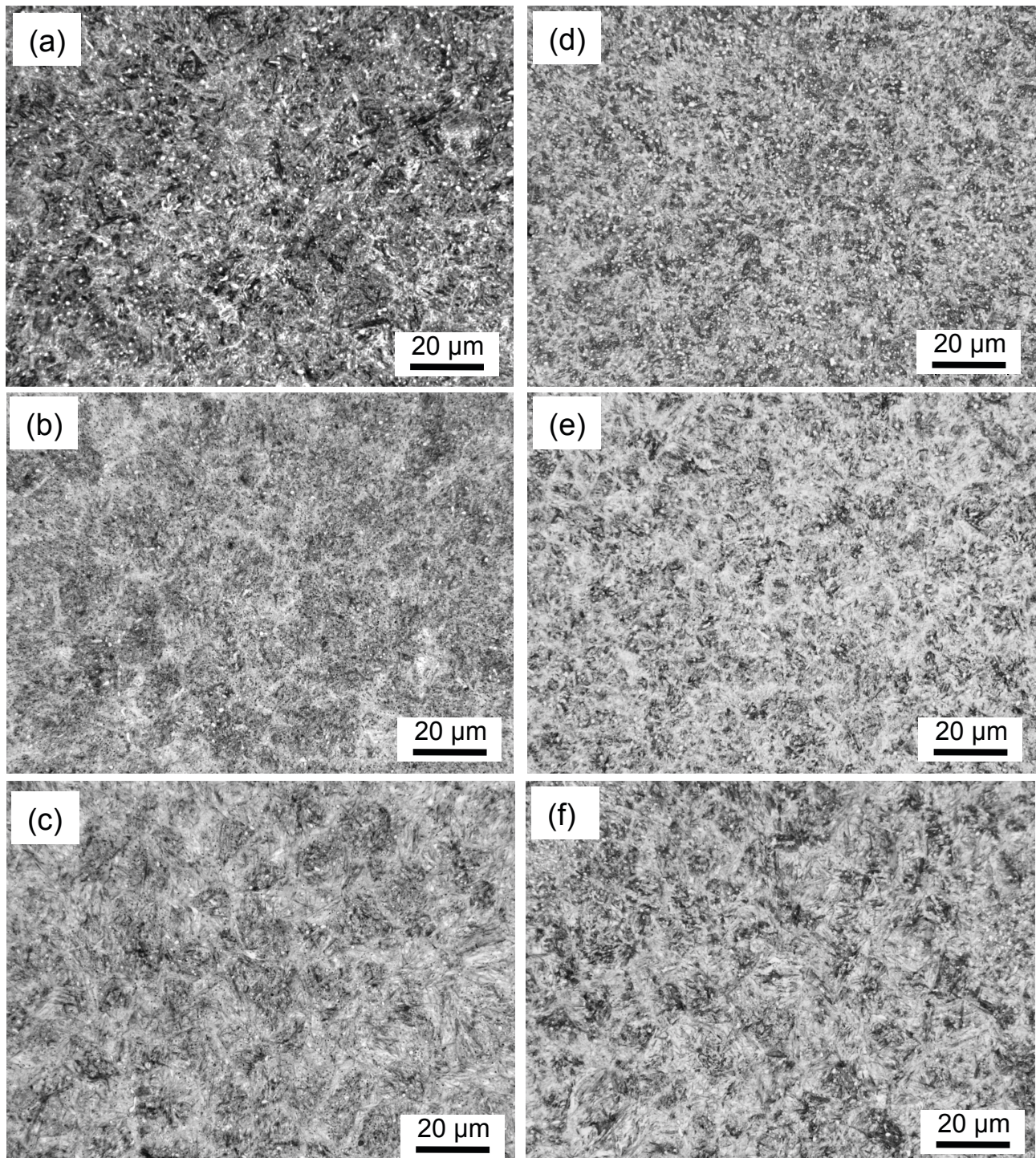
Figure 2: Optical metallography showing the microstructure of heat treated 100Cr6 (a) T_{aus}=820 °C (b) T_{aus}=860 °C (c) T_{aus}=900 °C, and 100CrMnSi6-4 (d) T_{aus}=800 °C (e) T_{aus}=840 °C (f) T_{aus}=880 °C.

3.2. Phase transformations overview from dilatometry

Dilatometric curves for the continuous heating and cooling experiment are plotted for 100Cr6 and 100CrMnSi6-4 in Figure 3a and b, respectively. In both grades, a transformation event associated with an increase in strain was observed upon heating. It is present consistently at around 250–300 °C for 100Cr6 samples and is located at comparatively high temperatures for 100CrMnSi6-4 samples. Whilst it is evident in 100Cr6 samples that the increase in strain weakened towards higher temperatures around 300 °C, as the slope became near horizontal, the phenomenon is not observed in 100CrMnSi6-4 samples, possibly due to the shift of the transformations to higher temperatures that were not covered in the experiment. Then, holding at 350 °C results in similar reductions in strain for all samples, which is likely associated with the precipitation of cementite. Upon cooling, no significant phase transformation was detected as the curves do not show inflexion points.

3.3. Reactions upon heating

Figure 4 gives the derivative of the heating range of each dilatometric curve for a closer examination of the slope variation as a function of temperature. Considering that all slopes have positive values, the derivative curve (plotted as scattered points) reflects a change in slope of its parent curve, in a way that it rises when the slope of the parent curve becomes more positive, falls as the slope became less positive, and remains constant when there is no variation in slope. Based on variations in the derivative curves, about 5 reaction stages were observed for 100Cr6 samples:

1. At temperatures below ∼160 °C, no phase transformations were expected and the strain should only be influenced by the thermal expansion effect. As a result, the derivative curve changes linearly with temperature.

2. Between 160 and 225 °C, a slight drop in the derivative curves is observed. A similar phenomenon has been reported upon tempering a hardened unalloyed high-carbon steel by Pacyna [35], in which a contraction in strain was observed right before a dilatation caused by retained austenite decomposition, and was associated with the precipitation
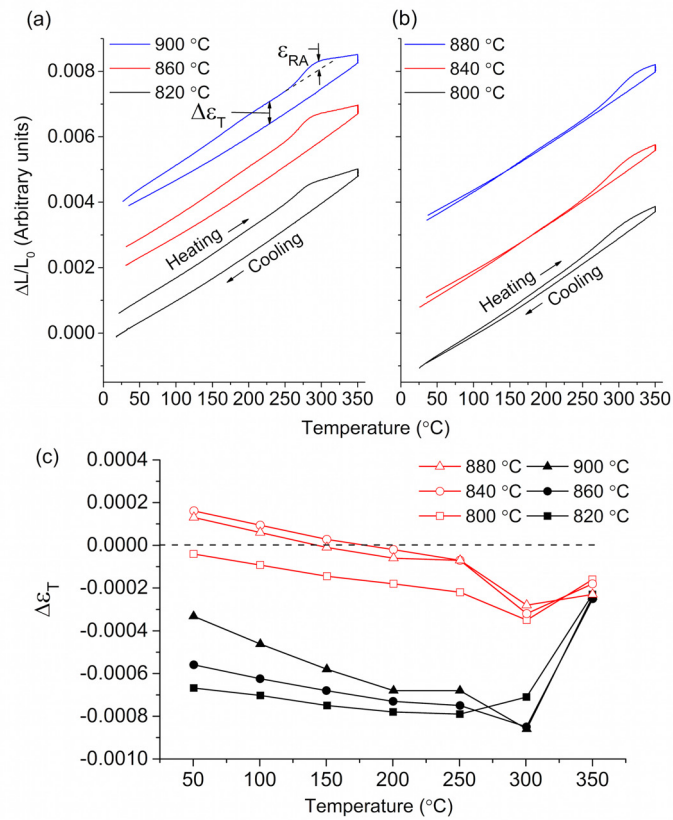
10

Figure 3: Dilatometric curves showing strain variations as a function of temperature for (a) 100Cr6 and (b) 100CrMnSi6-4; and (c) the strain difference $\Delta\varepsilon_T$ at temperatures between the heating and cooling dilatometric curves. $\varepsilon_{\mathrm{RA}}$, estimated transformation strain for retained austenite decomposition.
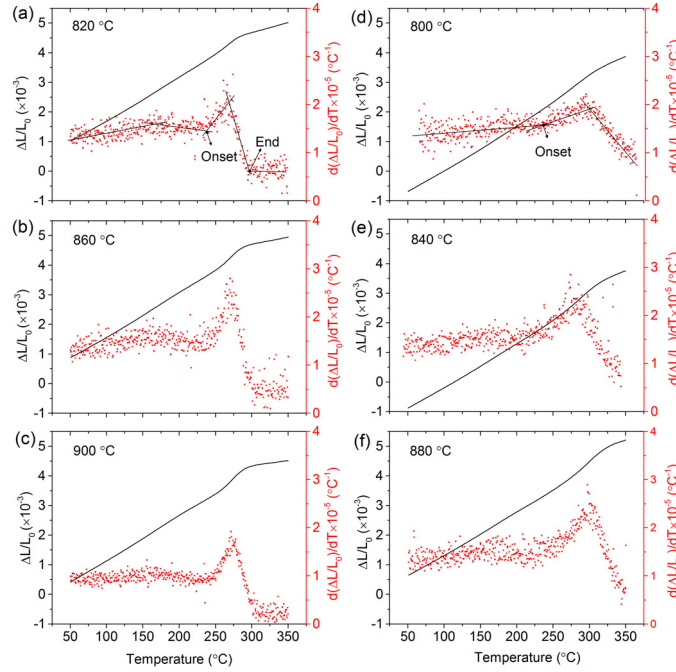
11

Figure 4: Plots showing the dilatometric curve (solid line) of 100Cr6 samples austenitised at (a) 820 °C (b) 860 °C (c) 900 °C and 100CrMnSi6-4 samples austenitised at (d) 800 °C (e) 840 °C (f) 880 °C upon heating, and their corresponding derivative curve (scattered points) showing the change in the slope on the dilatometric curve.

of transient carbides, mainly ϵ-carbide. The transition carbides were suggested to take carbon from supersaturated martensite, and precipitate at tempering temperatures up to 200 °C [36, 37]. Indeed, Barrow [38] has shown the precipitation of ϵ-carbide in 100Cr6 after 0.25 h tempering at 160 °C.

3. Then, retained austenite decomposition is observed up to 275 °C as the derivative curves increase sharply. The length change depends on the composition of austenite and the transformed amount. It should be noted that austenite decomposition may sometimes cause a net contraction when retained austenite is present at high carbon content, as reported in [39] for superbainitic steel containing 1.2 wt.% carbon.

4. The sharp rise in the derivative curve is followed by a steep decrease, at approximately 275–300 °C. This implies that although the slope of the curve remains positive, it levels up at elevated temperatures within the range. At this temperature range, the strain could be influenced by three effects:

12

(a) Thermal expansion that leads to an increase in strain at elevated temperature. The increment in strain, however, changes when there are microstructural alterations. In this experiment, the decomposition of retained austenite results in a decrease in the content of retained austenite, and an increase in ferrite content. The thermal expansion coefficient of ferrite, however, is low in comparison to that of retained austenite [23]. As a result, the overall thermal expansion coefficient decreases, causing decreasing increments in strain.

(b) Continuous decomposition of retained austenite leading to a dilatation effect. However, such dilatation could fade gradually, as early decomposed retained austenite could reject carbon into the surrounding retained austenite, increasing the stability of retained austenite.

(c) Contraction [35] caused by cementite formation. This reaction might overlap with the previous stages, as the formation of cementite in unalloyed high-carbon steels during tempering initiates at ∼200 °C [35].

5. Above ∼300 °C, the derivative curves become steady again, which suggests the absence of significant further phase transformations.

100CrMnSi6-4 samples, by contrast, show only stage 1, 3 and 4 as described above, Figure 4d–f. Whilst the absence of Stage 5 can be easily explained as being postponed to higher temperatures, the reason for the missing Stage 2 requires information on the formation of ϵ-carbide in 100CrMnSi6-4 martensitic bearing steels, which is rather limited in the open literature. A possibility would be that the increased Si content retards ϵ-carbide formation; possibly inhibiting it at this heating rate.

It is also noted that the peaks corresponding to Stage 3 and 4 in 100Cr6 samples are much sharper, covering a narrower temperature range than those in 100CrMnSi6-4. The approximate temperature range was measured by an onset temperature and an end temperature illustrated in Figure 4a and d. For 100CrMnSi6-4 samples, only the onset temperature was estimated, and the end temperature is above 350 °C for all samples. The temperature

13

range was measured as a rough evaluation of retained austenite decomposition, it should be noted that uncertainty for the onset and end temperatures can be caused when the retained austenite transformation is overlapped with other transients. Nevertheless, 100CrMnSi6-4 shows a wider gap.

3.4. Phase transformation strains

The positive strain ($\varepsilon_{\mathrm{RA}}$) caused by retained austenite decomposition was estimated by extending the near linear part of the dilatation curve and measuring the maximum strain difference between the extended curve and the dilatation curve, as demonstrated in Figure 3a. The results are summarised in Table 3 and indicate that the magnitude of the strain is in the order of 10^{-4} for all samples.

Table 3: Dilatometry measurements on the strain $\varepsilon_{\mathrm{RA}}$ caused by retained austenite transformation.

	100Cr6		100CrMnSi6-4
T_{aus}, °C	strain ($\varepsilon_{\mathrm{RA}}$)	T_{aus}, °C	strain ($\varepsilon_{\mathrm{RA}}$)
820	0.0001(1)	800	0.0002(1)
860	0.0002(1)	840	0.0003(3)
900	0.0002(3)	880	0.0003(5)

Another distinct phenomenon derived from Figure 3a and b is the strain difference ($\Delta\varepsilon_T$) between the heating and the cooling curves, as illustrated in Figure 3a. Measurements for the strain difference as a function of temperature are shown in Figure 3c. Although retained austenite decomposition causes expansion in sample length, most samples show a net contraction following the implemented heating and cooling procedure, as the strain values are negative. The contraction is mainly caused by Stage 4, which is not fully revealed in 100CrMnSi6-4 samples; as a result, the contraction is less prominent in these samples than in 100Cr6 samples. Also, a large contraction is observed in samples austenitised at low temperatures, 800 °C for 100CrMnSi6-4 and 820 °C for 100Cr6, for instance. This can be explained as the contraction being neutralised by an expansion caused by retained austenite decomposition. Samples austenitised at lower temperatures have less retained austenite than high T_{aus} samples and thus have less neutralisation effect. Due to this effect, retained

14

austenite decomposition can promote the strain stability of specimens by cancelling out the contraction arising from Stage 4 in this particular case.

3.5. Phase evolution from synchrotron spectra

The evolution of the diffraction pattern at elevated temperatures for all samples is plotted in Figure 5. Unfortunately, *in situ* spectra for the 820 °C sample were not obtained due to sample holder failure. Data on this sample were thus based on diffraction patterns collected from the reference samples and a trial scan. The decomposition of retained austenite has been observed across all samples as the gradual disappearance of austenite peaks, the first five of which are labelled in the plot as γ_{111}, γ_{200}, γ_{220}, γ_{311} and γ_{222}.

For 100Cr6 samples (Figure 5a and b), the austenite decomposition was most evident from 300 to 350 °C. It was accompanied by a consistent increase in ferrite peak intensity, and the subsequent development of cementite peaks which became visible from 350 °C onwards. Each of the ferrite peaks appears to be symmetric across the spectra; and they became sharper upon heating, likely due to the relief of residual stress. Also, a small bump appears at a 2θ value right under 40° for all samples, and it became sharper at the elevated temperature, and most prominent at 500 °C. As the peak is present at all temperatures and shows a severe broadening, it is likely generated from fine size temper carbides, which have been reported to be elongated cementite of tens of nanometres in size [40], and are often present at grain boundaries or inside martensite plates.

For 100CrMnSi6-4 samples (Figure 5c–e), unexpected austenite peak splitting has been observed on 840 and 880 °C samples. For the purpose of this discussion, the low angle split peak is denoted as γ, whilst its high angle counterpart is defined as γ'. Whilst retained austenite decomposition was observed as a decrease of the γ peaks on all 100CrMnSi6-4 samples, the presence of the γ' is less understood, with an attempted interpretation presented in Section 3.9. The reduction in the γ peak intensity became most evident at 350–400 °C, in comparison to 300–350 °C for 100Cr6 samples. Similar to 100Cr6 samples, the ferrite peaks increase as the retained austenite decomposes and cementite development became
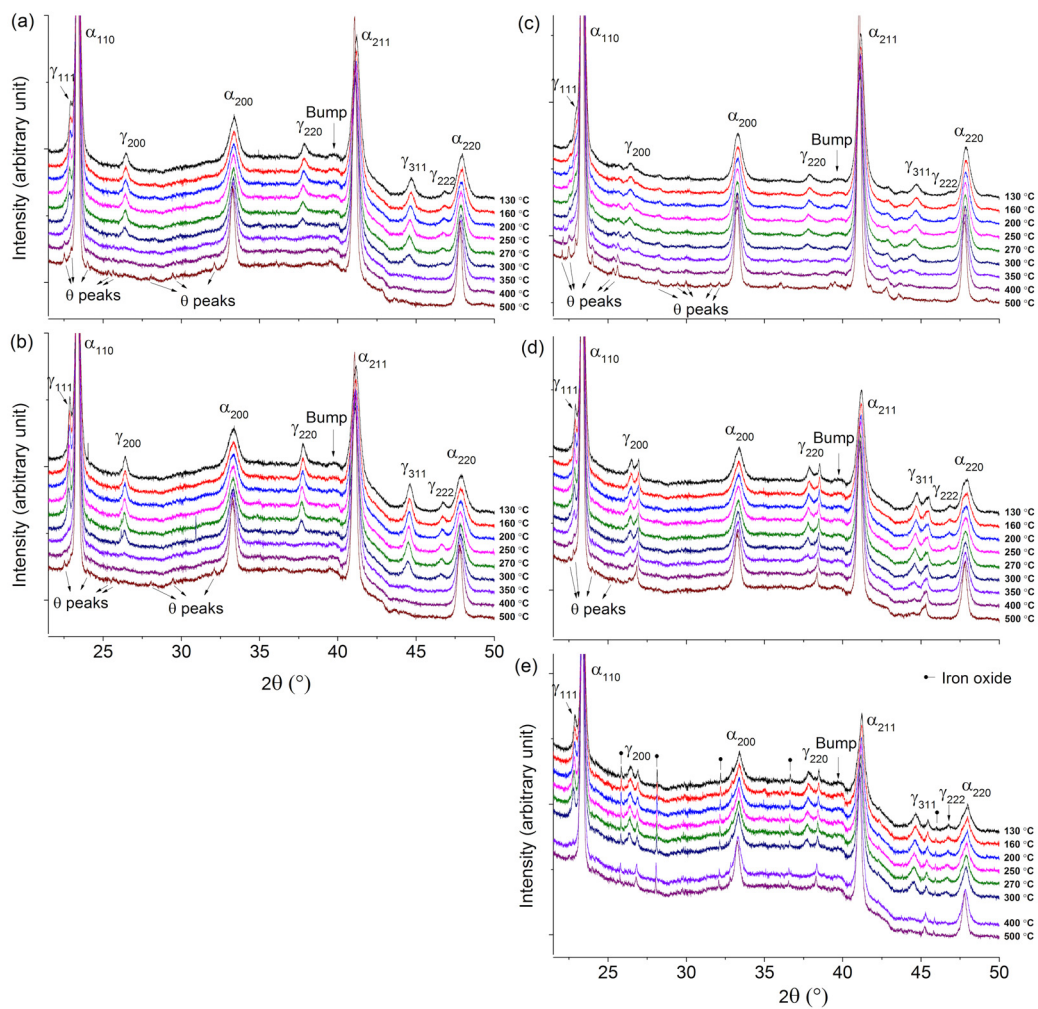
Figure 5: The evolution of synchrotron spectrum at elevated temperatures for 100Cr6 austenitised at (a) 860 °C and (b) 900 °C, and for 100CrMnSi6-4 austenitised at (c) 800 °C (d) 840 °C and (e) 880 °C. Note that spectrum at 350 °C is not obtained for 880 °C due to an experimental failure.

16

prominent at temperatures of ~350 °C. Also, it is noted that ferrite peaks appear broader for high T_{aus} samples than those with low T_{aus}, possibly due to the higher residual stress generated during quenching. In addition to the broadening, each of the peaks obtained from the high T_{aus} samples appear to be less symmetric, likely due to the presence of non-uniformly distributed dislocations or localised lattice distortion, and could also stem from the BCT structure of martensite formed upon quenching. The peaks became sharper and more symmetric at high temperatures which allows some relief of residual stress, redistribution of carbon in martensite and dislocations. Moreover, the bump observed at 39–40° in Figure 5c–e developed into several peaks corresponding to cementite peaks at 500 °C, most obvious from the 820 °C sample, further supporting the assumption that the bump was a result of fine cementite particles.

Phase evolution was quantified via Rietveld refinement and is plotted in Figure 6a–c for 100Cr6 samples, and d–f for 100CrMnSi6-4. The room temperature austenite contents were approximately 16 wt.%[1] for both the 100Cr6 860 and 900 °C specimens, similar to the 100CrMnSi6-4 840 and 880 °C specimens. Whilst the 820 and 800 °C samples show relatively lower retained austenite quantities, of 7 wt.% and 12 wt.%, respectively. For both grades retained austenite remained stable until 200–250 °C, thereon reducing dramatically until a full decomposition. The ferrite phase amount increased together with retained austenite decomposition, reaching values up to 95 wt.% in some specimens. Cementite, in most cases, remained stable at ~4 wt.% from room temperature up to 350 °C, and it increased by ~2–4 wt.% at higher temperatures. From 400 °C onwards, whilst about 3 wt.% retained austenite was left in the 840 °C sample, complete decomposition was achieved on all other specimens.

The onset and end temperature for retained austenite decomposition estimated from synchrotron spectra show good agreement with the dilatometry results, as shown in Fig-

---

[1]Phase weight percentages are nearly identical to volume percentages for cementite, ferrite/tempered-martensite and austenite as the densities of these phases are nearly the same.
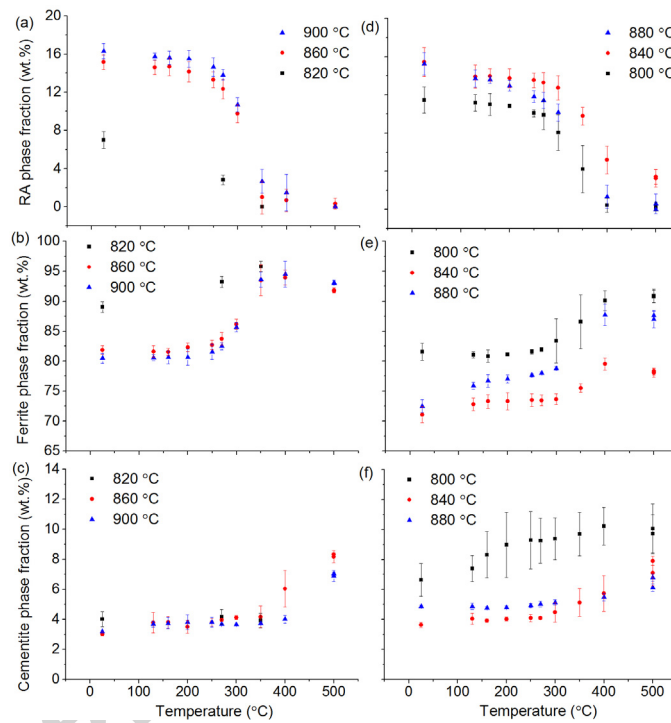
Figure 6: The evolution of the phase quantities of (a) austenite (b) ferrite and (c) cementite in 100Cr6, and (d) austenite (e) ferrite and (f) cementite in 100CrMnSi6-4. Retained austenite fractions for peak splitting specimens were determined from the γ peaks. Errors are standard deviation of multiple fitting results. The room temperature data for the 820 °C specimen was determined via a trial scan and a magnetic saturation measurement on the retained austenite content. RA refers to retained austenite.

18

ure 7a. A significant variation of at least 50 °C in the end temperature between the two grades was prominent, implying that higher energy is required to fully decompose retained austenite in 100CrMnSi6-4 compared to 100Cr6. A possible reason could be that the high Si content in 100CrMnSi6-4 retards retained austenite decomposition by inhibiting cementite precipitation [41].
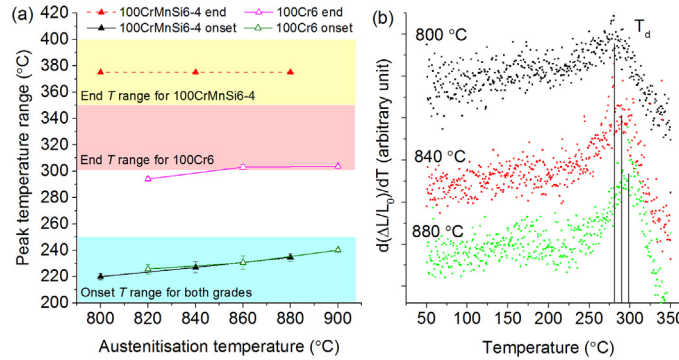

Figure 7: (a) Dilatometry (data points) and synchrotron (coloured sections) values for the onset and end temperature of retained austenite decomposition; and (b) derivative curves showing the shift of T_d point to high temperature for high T_{aus} samples Note that data on the dashed line were estimated to be above 350 °C, but an exact temperature was not observed as 350 °C was the highest temperature reached.

In addition, it is noticed that cementite development was more prominent at the low T_{aus} sample than the high T_{aus} sample in both grades. Dilatometry results (Figure 7b) show that the temperature T_d corresponding to the initial drop after retained austenite decomposition in the derivative curves shifts to high temperature for high T_{aus} samples, suggesting that the precipitation and growth of cementite in high T_{aus} samples could be delayed to high temperatures.

It is concluded that retained austenite in 100Cr6 and 100CrMnSi6-4 martensitic bearing steels is thermally unstable at elevated temperatures. At a heating rate of approximately 0.05 °C/s, its decomposition initiates at temperatures between 200 and 250 °C for both materials, and continued until retained austenite fully decomposes. A complete decomposition was achieved at the temperature range of 300–350 °C for 100Cr6, and it is retarded to a higher temperature range of 350–400 °C for 100CrMnSi6-4. The decomposition is accompanied by an increase in ferrite and cementite contents. Also, it is worth noticing that the

19

decomposition of the unstable retained austenite could be completed in less than 1 h at this heating rate.

3.6. Room temperature lattice constants and carbon contents

Table 4 and Table 5 give the initial lattice parameters and carbon concentrations for retained austenite and tempered-martensite measured from spectra collected at room temperature. For 100Cr6, the retained austenite lattice parameter was greater for the sample austenitised at 900 °C (0.3595(6) nm) than 860 °C (0.3590(5) nm), Table 4. The values are consistent with the literature [23], in which 0.35951 (900 °C) and 0.35892 nm (860 °C) were reported. Similarly, the tempered-martensite lattice expanded at the increasing T_{aus}, and has values in good agreement with reported values of 0.28706 nm (860 °C) and 0.28718 nm (900 °C) [23]. The carbon concentration increases consistently with the expanding lattices, appearing higher in phases obtained at high T_{aus} than low T_{aus}. An increase of T_{aus} from 860 °C to 900 °C has yielded about 0.1 wt.% increase in the carbon concentration for both phases.

100CrMnSi6-4 samples appear to have similar lattice parameters and carbon concentrations to 100Cr6 samples austenitised at 20 °C higher in the ranges 0.3588(6)–0.3593(9) nm, and 0.69–0.81 wt.%, respectively, as shown in Table 5. The lattice constant of tempered-martensite, although appears to be constant regardless of T_{aus}, has values (0.2870 nm) comparable to 100Cr6. In contrast to retained austenite, the carbon content in the tempered-martensite is low, ranging 0.1–0.2 wt.% for all samples.

Table 4: Room temperature lattice parameters and carbon contents prior to the *in situ* experiments for 100Cr6.

T_{aus}, °C	820	860	900
Retained austenite lattice (nm)	-	0.3590(5)	0.3595(6)
Tempered-martensite lattice (nm)	0.2867(0)	0.2869(7)	0.2871(1)
C content in retained austenite (wt.%)	-	0.74	0.85
C content in tempered-martensite (wt.%)	0.02	0.16	0.24

20

Table 5: Room temperature lattice parameters and carbon contents prior to the *in situ* experiments for 100CrMnSi6-4.

T_{aus}, °C	800	840	880
Retained austenite lattice (nm)	0.3588(6)	0.3589(4)	0.3593(9)
Tempered-martensite lattice (nm)	0.2870(6)	0.2870(4)	0.2869(0)
C content in retained austenite (wt.%)	0.69	0.70	0.81
C content in tempered-martensite (wt.%)	0.19	0.18	0.10

3.7. In situ *carbon content and lattice evolution*

During the *in situ* experiment, shifts of peak positions were observed as a result of lattice dimensional changes under continuous heating. An expansion in the austenite or ferrite lattice results in a cooperative shift of its peaks to lower angles. The measured evolution of lattice parameters for austenite and ferrite is given in Figure 8. Both austenite and ferrite expand with increasing temperature. The lattice variations, however, are the result of two influences: thermal expansion and the redistribution of solute atoms. The former causes lattice dilatation upon continuous heating; its magnitude is determined by the thermal expansivity of the material. The latter could result in either shrinkage or expansion of the lattice, depending on the type of solute and its redistribution path. Whilst substitutional alloying elements have much lower diffusivity in austenite, for instance, ranging from 10^{-29} to 10^{-31} m^{2}s^{-1} at 300 °C in comparison to a carbon diffusivity of 8×10^{-19} m^{2}s^{-1} [42], and have a moderate effect on the lattice owing to their low concentration, its effect on the lattice variations was assumed negligible. The effect of carbon on the lattice variations was estimated by subtracting the thermal expansion effect from the experimentally measured values. The redistributed carbon concentration in the tempered-martensite and austenite can be calculated from Equations 5 and 6, which are derived from Equations 3 and 4, respectively.

$$C_c = \frac{a_\alpha(E) - a_\alpha(T)}{0.002} \tag{5}$$

$$C_c = \frac{a_\gamma(E) - a_\gamma(T)}{0.00453} \tag{6}$$

where $a_\alpha(E)$ is the experimentally measured lattice parameter for ferrite; $a_\alpha(T)$ is the ferrite lattice parameter under pure thermal expansion effect; $a_\gamma(E)$ and $a_\gamma(T)$ are those for austenite. 0.002 and 0.00453 are the factors for carbon shown in Equations 3 and 4. All lattice values are in nanometres in these equations.
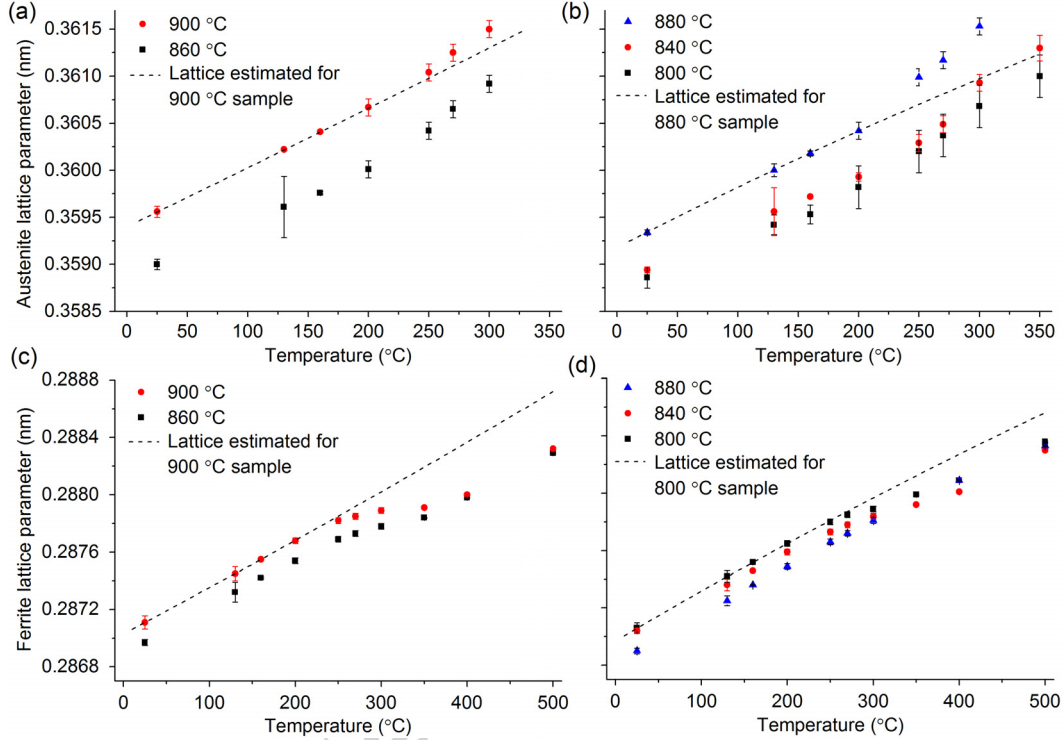

Figure 8: Evolution of lattice parameters for (a) austenite in 100Cr6 and (b) 100CrMnSi6-4; (c) ferrite in 100Cr6, and (d) 100CrMnSi6-4. The dashed curve in each plot is the estimated lattice change under pure thermal influence estimated using Equation 7. Error bars are standard deviation of multiple fitting results, and those smaller than the data markers are invisible.

Under 160 °C, no phase transformation was detected from the synchrotron experiments. It is then expected that phase lattices expand solely under thermal effects, which can be expressed as a function of temperature in a quadratic equation [23]:

$$a(T) = AT^2 + BT + C \tag{7}$$

The lattice parameters obtained at 25, 130 and 160 °C were fitted quadratically, with the fitting parameters A, B and C listed in Table 6. The fit curves show the prediction of lattice changes under pure thermal effects, and examples are displayed in Figure 8 for each

plot. It is observed that the lattices deviate from the fitting curves at high temperatures for both phases. Whilst retained austenite lattices deviates from the dashed line to high values, ferrite lattices go below the dashed line, as observed by comparing Figure 8a and b to Figure 8c and d.

Table 6: Fitting results of parameters A, B and C for Equation 7 to describe lattice parameter variations of the corresponding phases.

Sample	Retained austenite fitting			Ferrite fitting		
	A ($\times 10^{-9}$)	B ($\times 10^{-6}$)	C	A ($\times 10^{-9}$)	B ($\times 10^{-6}$)	C
860 °C	−5.9965	6.7390	0.35884	0.3175	3.2746	0.28689
900 °C	0.3527	6.2310	0.35940	0.3880	3.1875	0.28703
800 °C	−12.346	7.2469	0.35869	−0.7055	3.5379	0.28970
840 °C	−4.2304	6.5474	0.35878	0.8818	2.9109	0.28697
880 °C	−2.1164	6.6138	0.35918	0.0247	3.4028	0.28681

The evolution of carbon concentration upon heating in austenite and ferrite is shown in Figure 9, the errors were determined from multi-measurements of the experimental lattice parameters. The carbon present in retained austenite remained stable at temperatures below 160 °C, and increased to a maximum of 0.85–0.90 wt.% until retained austenite fully decomposed. The increments in carbon content in weight percentage are 0.13 (860 °C) and 0.04 (900 °C) for 100Cr6; 0.27 (800 °C), 0.13 (840 °C) and 0.12 (880 °C) for 100CrMnSi6-4. On the contrary, the carbon in the ferrite continuously decreased with increasing temperature.

3.8. Thermal expansion coefficients

The mean coefficients of linear thermal expansion α_m of the heat-treated materials from room temperature to 150 °C range were measured on the dilatometry curves, employing equation [43]:

$$\alpha_m = \frac{1}{L_0}\frac{\Delta L}{\Delta T} \tag{8}$$

where L_0 is the initial length of specimens at room temperature, ΔL and ΔT are the changes in length and temperature, respectively. The results are summarised in Table 7, α_m of about 14×10^{-6} K^{-1} is yielded for the mixed microstructure of tempered martensite, retained austenite and cementite of the heat-treated samples.
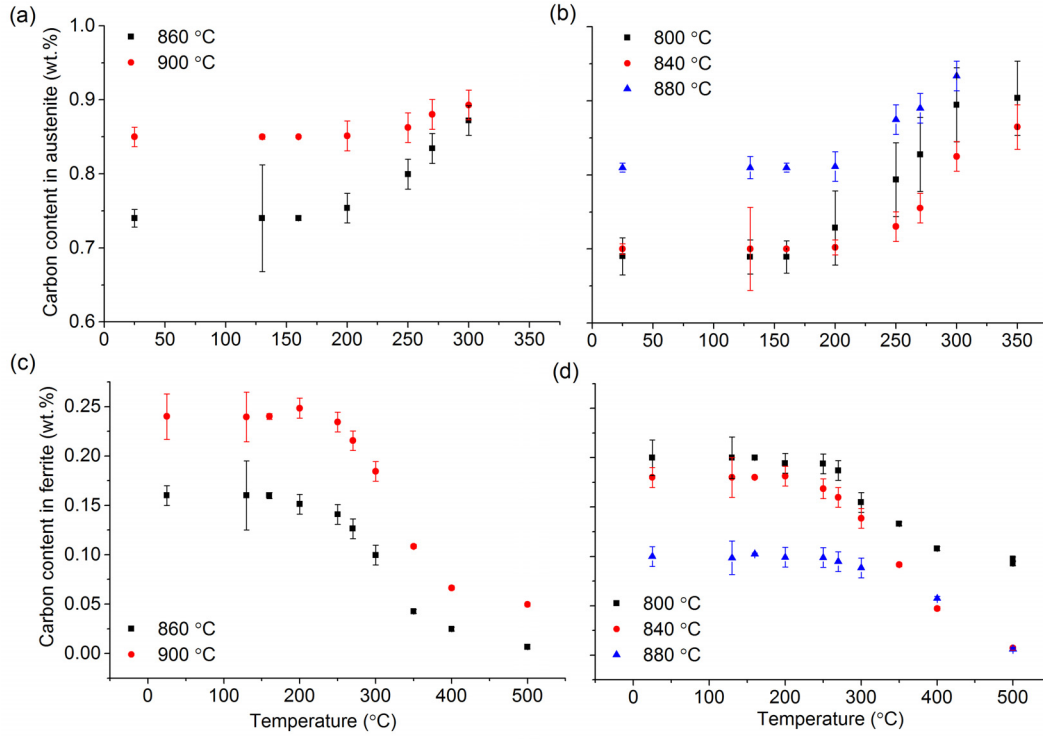
Figure 9: The evolution of carbon concentration for austenite in (a) 100Cr6 and (b) 100CrMnSi6-4, and for ferrite in (c) 100Cr6, and (d) 100CrMnSi6-4. Error bars are standard deviation of multiple results.

Table 7: Mean coefficients of linear thermal expansion derived from ASTM E228 [43], from room temperature to 150 °C temperature range for the heat-treated specimens. Errors are estimated from multiple measurements at a temperature range of ± 5 °C.

Sample	α_m, $\times 10^{-6}$ K^{-1}	Sample	α_m, $\times 10^{-6}$ K^{-1}
820 °C	14.0±0.05	800 °C	14.3±0.05
860 °C	14.0±0.04	840 °C	14.2±0.15
900 °C	15.0±0.04	880 °C	13.8±0.21

Also, Table 8 summarises the room temperature thermal expansion coefficient for austenite and tempered-martensite phases, estimated via Equation 9 [44]. Results are consistent with the published values of 18.1×10^{-6} and 12.6×10^{-6} at 20 °C for austenite and ferrite, respectively [23]. Additionally, the experimentally determined thermal expansion coefficients of the bulk shown in Table 8 are in line with the rule of mixtures for a mixed structure of retained austenite and ferrite, assuming that cementite has no influence due to its small amount.

$$\alpha_T = \frac{1}{a}\frac{\delta a}{\delta T} \tag{9}$$

where α_T is the instantaneous coefficient of thermal expansion at temperature T, the lattice constant a is a function of temperature T, as expressed in Equation 7.

Table 8: Thermal expansivity at 25 °C calculated from Equation 9.

Sample	α_T at 25 °C (K^{-1})	
	Retained austenite	Tempered-martensite
860 °C	17.9×10^{-6}	11.5×10^{-6}
900 °C	17.4×10^{-6}	11.2×10^{-6}
800 °C	18.5×10^{-6}	12.2×10^{-6}
840 °C	17.7×10^{-6}	10.3×10^{-6}
880 °C	18.1×10^{-6}	11.8×10^{-6}
Average	17.9×10^{-6}	11.4×10^{-6}

3.9. Peak splitting

In our experiment, austenite peaks in some cases appeared in pairs, Figure 5d and e. The splitting phenomenon has been ascribed in few reports [42, 45] to the presence of retained austenite of different carbon contents or morphologies (film and block). Nevertheless, the peaks in this study are much more separated compared to the earlier observations in the literature.

The influence from the sample holder can be ruled out for such phenomenon, as all samples are assembled in a standard way, whilst only certain samples show the splitting of austenite peaks. Also, these samples have been moved away after the room temperature

25

scans, and then placed back for the *in situ* experiment. The fact that other spectra collected in between these experiments show no appearance of peak splitting suggests that the splitting peaks were likely a result from the specimens. Moreover, the fact that the splitting peaks are well-formed with a good number of data points, suggesting that the associated phases are not an artifact. In addition to that, the splitting peaks appear on spectra collected at room temperature prior to the *in situ* experiment and thus are not a consequence of the *in situ* experiment.

It is observed that the peaks differ from not only the peak position, but also the peak intensity and shape:

- The γ' peaks have relatively lower intensity than the γ peaks, and could account for an extra austenite amount of 9.5±0.7 wt.% and 5.7±0.7 wt.% in the 840 °C and 880 °C samples, respectively. More importantly, whilst γ peaks appear unstable and reduced in intensity upon heating, γ' peaks appeared to be thermally stable at temperatures up to 500 °C.

- Whilst γ yields room temperature lattice constants of 0.3589(4) nm and 0.3593(9) nm for the 840 and 880 °C samples, respectively, γ' has unexpectedly small lattice parameters of 0.3537(1) nm and 0.3538(3) nm, which are smaller than the reported lattice parameters of 0.3556 nm [4] for pure FCC-iron. The exact reason for this remains unclear, but it is noticed in the literature that lattice parameters could have an uncertainty of the order of magnitude of 10^{-3} nm, for example, the lattice for pure FCC-iron has been reported to be 0.3556 nm [4], 0.35669 nm [46] and 0.35780 nm [42]. Another possible reason for the extremely small lattice parameter of γ' is that the peaks shift to high angles as a result of grains being strained compressively [47]. Moreover, the addition of Si could contract further the austenite lattice. Nevertheless, the difference in lattice parameters could suggest the presence of austenite of different carbon contents.

- The γ peaks are broader than γ' peaks, as a broadening effect[2] from either small crystallite

---

[2]Instrumental broadening, which was measured to be 0.03° from the full width at half maximum of peaks

size or the presence of non-uniform microstrain, or a combination of both factors. Also, γ' peaks appear to be less symmetric, possibly due to the presence of internal stress or dislocation structures within the grains. These, could further contribute to the different stabilities of the splitting peaks upon heating.

4. Conclusions

This work examines austenite stability at continuous heating up to 500 °C at ~0.05 °C/s for martensitic bearing steel grades 100Cr6 and 100CrMnSi6-4. Strains associated with austenite transformation were revealed by diltometry. The transformation mechanisms, as well as evolution in the phase contents, lattice constant and carbon content at elevated temperature were *in situ* investigated via synchrotron. The results are compared for the two grades of different Mn and Si contents, with key results summarised as below:

- Retained austenite in both 100Cr6 and 100CrMnSi6-4 martensitic bearing steels is unstable upon heating. The transformation initiates at approximately 225 °C for both grades, whilst there is large variation in their end temperature, which ranges 300–350 °C for 100Cr6, and 350–400 °C for 100CrMnSi6-4. This implies that retained austenite in 100CrMnSi6-4 is more thermally stable than that in 100Cr6 and thus requires higher energy or time for full decomposition. Also, once sufficient temperature has been reached, the complete decomposition of retained austenite could take less than an hour.

- The decomposition of retained austenite upon heating was observed to be accompanied by an enrichment of carbon in the austenite phase. At the same time, there was an increase in the tempered-martensite/ferrite phase with a reduction in its carbon content. The development of cementite was detected only above 300 °C.

- The transformation of retained austenite upon both heating and cooling results in an expansive strain in the magnitude of 10^{-4}. Such strain can be neutralised by contrac-

---

collected from a standard Si sample, is neglected as being an order of magnitude lower than that of the collected peaks.

tions occurred at high temperatures ($>\sim 300$ °C) caused by reactions such as cementite precipitation.

- In some cases, the austenite exhibited pairs of peaks γ and γ', the reason for which has yet to be established, but could be related to differences in solute content. In spite of peak position, the pairs of peaks also differ in peak shape and peak stability, suggesting γ and γ' of different structures and thermal stabilities. However, the abnormal small lattice parameter measured for γ' needs further explanation.

- The mean coefficient of linear thermal expansion for all 100Cr6 and 100CrMnSi6-4 samples was about 14×10^{-6} K^{-1}, for the temperature range covering room temperature to 150 °C. The respective thermal expansivities at 25 °C for austenite and tempered-martensite were approximately 17.9×10^{-6} K^{-1} and 11.4×10^{-6} K^{-1}.

5. Acknowledgements

[1] E. M. Lips, H. Van Zuilen, Improved hardening technique, Metal Progress 66 (1954) 103.

[2] I. Gokyu, J. Kihara, T. Kishi, The strengthening mechanism of ausformed martensitic steel, J. Japan Inst. Metals 31 (1967) 1176–1180.

[3] V. F. Zackay, E. R. Parker, The changing role of metastable austenite in the design of alloys, Annual Review of Materials Science 6 (1976) 139–155.

[4] H. K. D. H. Bhadeshia, R. W. K. Honeycombe, Steels microstructure and properties, 3rd ed., Butterworth-Heinemann, Oxford, UK, 2006.

[5] V. F. Zackay, E. R. Parker, D. Fahr, R. Busch, The enhancement of ductility in high-strength steels, ASM Transaction 60 (1967) 252–259.

[6] B. C. De Cooman, Structure–properties relationship in TRIP steels containing carbide-free bainite, Current Opinion in Solid State and Materials Science 8 (2004) 285–303.

[7] B. L. Averbach, M. Cohen, S. G. Fletcher, The dimensional stability of steel: part III. decomposition of martensite and austenite at room temperature, ASM Transaction 40 (1948) 728–743.

[8] W. Luty, Influence of heat treatment on the dimensional stability of bearing rings of steel 100Cr6 and 100MnCr6 at room temperature and at 150 °C, Härterei-technische Mitteilungen 27 (1972) 27–33.

[9] F. Hengerer, W. Nierlich, J. Volkmuth, H. Nützel, Dimensional stability of high carbon bearing steels, Ball Bearing Journal 231 (1988) 26–31.

[10] P. K. Pearson, Size change of through hardened bearing steels at application temperatures, SAE Transactions A 106 (1997) 170–175.

[11] J. J. Bush, W. L. Grube, G. H. Robinson, Microstructural and residual stress changes in hardened steel due to rolling contact, ASM Transaction 54 (1961) 390–412.

[12] D. Zhu, F. X. Wang, Q. G. Cai, M. X. Zheng, Y. Q. Cheng, Effect of retained austenite on rolling element fatigue and its mechanism, Wear 105 (1985) 223–234.

[13] R. C. Dommarco, K. J. Kozaczek, P. C. Bastias, G. T. Hahn, C. A. Rubin, Residual stresses and retained austenite evolution in SAE 52100 steel under non-ideal rolling contact loading, Wear 257 (2004) 1081–1088.

[14] H. J. Böhmer, R. Eberhard, Microstructural optimisation of bearing steels for operation under contaminated lubrication by using the experimental method of dented surfaces,

in: J. Beswick (Ed.), Bearing steel technology, volume STP 1419, ASTM International, West Conshohocken, PA, 2002, pp. 244–262.

[15] K. Burkart, H. Bomas, R. Schroeder, H. W. Zoch, Rolling contact and compression-torsion fatigue of 52100 steel with special regard to carbide distribution, in: J. Beswick (Ed.), Advances in Rolling Contact Fatigue Strength Testing and Related Substitute Technologies, ASTM Int., West Conshohocken, PA, USA, 2012, pp. 218–236.

[16] S. Fujita, S. Matsuoka, T. Murakami, Effect of hydrogen on fatigue behaviour of bearing steel under cyclic torsion with compressive mean stress, in: Mechanics of Materials, Jpn. Soc. Mech. Eng., Tokyo, Japan, 2000, pp. 241–243.

[17] E. Joannides, A. P. Voskamp, G. E. Hollo, F. Hengerer, Fatigue behaviour of three variants of the roller bearing steel SAE 52100, in: E. Macherauch (Ed.), WerkstofSverhalten und Bauteilbemessung, DGM-Informationsgesellschaft, Oberursel, 1987, pp. 151–164.

[18] J. W. Kannel, S. A. Barber, Estimate of surface temperatures during rolling contact, Tribology Transactions 32 (1989) 305–310.

[19] E. Yajima, T. Miyazaki, T. Sugiyama, H. Terajima, Effects of retained austenite on the rolling fatigue life of ball bearing steels, Transactions JIM 15 (1974) 173–179.

[20] A. P. Voskamp, R. Österlund, P. C. Becker, O. Vingsbo, Gradual changes in residual stress and microstructure during contact fatigue in ball bearings, Journal of Metals Technology 7 (1980) 14–21.

[21] H. Muro, Y. Sadaoka, S. Ito, N. Tsushima, The effect of retained austenite on the rolling contact fatigue of carburized steels, Proceedings of the 12th Japan Congress on Materials Research–Metallic Materials March (1969) 74–77.

[22] H. Nakashina, Trends in materials and heat treatments for rolling bearings, NTN Technical Review 76 (2008) 10–17.

[23] E. Jimenez-Melero, R. Blondé, M. Y. Sherif, V. Honkimäki, N. H. van Dijk, Time-dependent synchrotron x-ray diffraction on the austenite decomposition kinetics in SAE 52100 bearing steel at elevated temperatures under tensile stress, Acta Materialia 61 (2013) 1154–1166.

[24] D. K. Bullens, Steel and its heat treatment, volume II—engineering and special purpose steels, John Wiley & Sons, Inc., New York, USA, 1939.

[25] W. Cui, Retained austenite in martensitic bearing steels, Ph.D. thesis, University of Cambridge, UK, 2017. In preparation.

[26] S. P. Thompson, J. E. Parker, J. Potter, T. P. Hill, A. Birt, T. M. Cobb, F. Yuan, C. C. Tang, Beamline I11 at Diamond: A new instrument for high resolution powder diffraction, Review of Scientific Instruments 80 (2009) 075107.

[27] H. M. Rietveld, A profile refinement method for nuclear and magnetic structures, Journal of applied Crystallography 2 (1969) 65–71.

[28] D. Fruchart, P. Chaudouet, R. Furchart, A. Rouault, J. P. Senateur, Etudes structurales de composés de type cémentite: Effet de l'hydrogène sur Fe_3C suivi par diffraction neutronique. Spectrométrie Mössbauer sur $FeCo_2B$ et Co_3B dopés au ^{57}Fe, Journal of Solid State Chemistry 51 (1984) 246–252.

[29] L. Cheng, A. Böttger, T. H. de Keijser, E. J. Mittemeijer, Lattice parameters of iron-carbon and iron-nitrogen martensites and austenites, Scripta Metallurgica et Materialia 24 (1990) 509–514.

[30] S. J. Lee, Y. K. Lee, Quantitative analyses of ferrite lattice parameter and solute Nb content in low carbon microalloyed steels, Scripta materialia 52 (2005) 973–976.

[31] N. H. van Dijk, A. M. Butt, L. Zhao, J. Sietsma, S. E. Offerman, J. P. Wright, S. van der

31

Zwaag, Thermal stability of retained austenite in TRIP steels studied by synchrotron X-ray diffraction during cooling, Acta Materialia 53 (2005) 5439–5447.

[32] MatCalc, `http://matcalc.tuwien.ac.at`, 1993.

[33] G. R. Lehnhoff, K. O. Findley, B. C. De Cooman, The influence of silicon and aluminum alloying on the lattice parameter and stacking fault energy of austenitic steel, Scripta Materialia 92 (2014) 19–22.

[34] D. J. Dyson, B. Holmes, Effect of alloying additions on the lattice parameter of austenite, Journal of the Iron Steel Institute 208 (2003) 469–474.

[35] J. Pacyna, Dilatometric investigations of phase transformations at heating and cooling of hardened, unalloyed, high carbon steels, Journal of Achievements in Materials and Manufacturing Engineering 46 (2011) 7–17.

[36] Y. Hirotsu, S. Nagakura, Crystal structure and morphology of the carbide precipitated from martensitic high carbon steel during the first stage of tempering, Acta Metallurgica 20 (1972) 645–655.

[37] F. H. Samuel, A. A. Hussein, Tempering of medium-and high-carbon martensites, Metallography 15 (1982) 391–408.

[38] A. T. W. Barrow, J.-H. Kang, P. E. J. Rivera-Díaz-del Castillo, The $\epsilon \to \eta \to \theta$ transition in 100cr6 and its effect on mechanical properties, Acta Materialia 60 (2012) 2805–2815.

[39] L. C. D. Fielding, E. J. Song, D. K. Han, H. K. D. H. Bhadeshia, D. W. Suh, Hydrogen diffusion and the percolation of austenite in nanostructured bainitic steel, Proceedings of the Royal Society of London A 470 (2014) 20140108.

[40] A. T. W. Barrow, P. E. J. Rivera-Díaz-del Castillo, Nanoprecipitation in bearing steels, Acta Materialia 59 (2011) 7155–7167.

[41] E. Kozeschnik, H. K. D. H. Bhadeshia, Influence of silicon on cementite precipitation in steels, Materials Science and Technology 24 (2008) 343–347.

[42] S. S. Babu, E. D. Specht, S. A. David, E. Karapetrova, P. Zschack, M. Peet, H. K. D. H. Bhadeshia, In-situ observations of lattice parameter fluctuations in austenite and transformation to bainite, Metallurgical and Materials Transactions A 36 (2005) 3281–3289.

[43] ASTM E228-11, Standard test method for linear thermal expansion of solid materials with a push-rod dilatometer, American Society for Testing and Materials, West Conshohocken, PA, 2011.

[44] G. W. C. Kaye, T. H. Laby, Tables of physical and chemical constants and some mathematical functions, 1995. http://www.kayelaby.npl.co.uk.

[45] A. S. Podder, I. Lonardelli, A. Molinari, H. K. D. H. Bhadeshia, Thermal stability of retained austenite in bainitic steel: an *in situ* study, Proceedings of the Royal Society A 467 (2011) 3141–3156.

[46] M. Onink, C. M. Brakman, F. D. Tichelaar, E. J. Mittemeijer, S. van der Zwaag, J. H. Root, N. B. konyer, The lattice parameters of austenite and ferrite in Fe-C alloys as functions of carbon concentration and temperatures, Scripta Metallurgica et Materialia 29 (1993) 1011–1016.

[47] B. D. Cullity, S. R. Stock, Elements of X-ray diffraction, 3rd ed., Prentice Hall, Oxford, UK, 2010.